Publications of the Astronomical Society of Australia (2026), **43**, e109, 15 pages
doi:10.1017/pasa.2026.10224

CAMBRIDGE UNIVERSITY PRESS

Research Article

Updating the PATH framework with FRB host galaxy models

Clancy W. James[1], Nick Loudas[2], Michele Woodland[3], Bridget C. Andersen[3], Xavier Prochaska[3,4,5], Jordan Luke Hoffmann[1], Lachlan Marnoch[6,7,8] and Stuart Ryder[6,7]

[1]International Centre for Radio Astronomy Research, Curtin University, Australia, [2]Department of Astrophysical Sciences, Peyton Hall, Princeton University, USA, [3]Department of Astronomy and Astrophysics, University of California Santa Cruz, USA, [4]Kavli Institute for the Physics and Mathematics of the Universe, Kashiwanoha, Kashiwa, Japan, [5]Division of Science, National Astronomical Observatory of Japan, Osawa, Mitaka, Tokyo, Japan, [6]School of Mathematical and Physical Sciences, Macquarie University, Australia, [7]Astrophysics and Space Technologies Research Centre, Macquarie University, Sydney, NSW, Australia and [8]Australia Telescope National Facility, CSIRO Space & Astronomy, Epping, NSW, Australia

Abstract

Identification of fast radio burst (FRB) host enables comparisons of host redshift with FRB dispersion measure to study the cosmological distribution of ionised gas, and analyses of host properties in order to identify FRB progenitors. In this work, we extend the Probabilistic Association of Transients to their Hosts (PATH) framework to incorporate physically-motivated priors on FRB host galaxy magnitudes. We develop three models for the apparent r-band magnitude distribution based on an FRB's expected host galaxy redshift, $P(m_r|z)$ and combine these with expectations for redshift based on an FRB's DM, $P(z|\mathrm{DM})$. We fit the parameters of these prior models using host galaxy candidates for 32 FRBs detected by the Australian SKA Pathfinder (ASKAP). We find increased confidence in the most probable hosts of all ASKAP ICS FRB host galaxies. All three models predict similar distributions of FRB host magnitudes at low redshift ($z \sim 0.1$), and we confirm previous results that the true FRB host galaxy distribution is fainter than expected for a star-formation-weighted distribution (p-value of 0.12%). However, a mass-weighted distribution provides an even worse fit (p-value of 10^{-9}). Tests against more FRBs in the $z > 0.5$ range, where the models differ, and extensions of the models to account for, for example, host metallicity, may help to resolve these uncertainties in the FRB host distribution.

Keywords: Radio transient sources; radio bursts; galaxies

(Received 2 April 2026 UTC; revised 27 May 2026 UTC; accepted 29 May 2026 UTC)

1. Introduction

Fast radio bursts (FRBs) are extremely energetic radio transients that reach the Earth from cosmological distances (Lorimer et al. 2007). Their most likely origin is in highly magnetised neutron stars, due to the extreme energy of their bursts (Ryder et al. 2023), micro-second time-structures (Farah et al. 2018), extreme magneto-ionic environments (Michilli et al. 2018), and the bright radio flares observed from the Galactic magnetar SGR 1935+2154 (Bochenek et al. 2020; CHIME/FRB Collaboration et al. 2020). However, their local environments range from extremely bright persistent radio sources (PRSs) located in dwarf, star-forming galaxies (Chatterjee et al. 2017; Niu et al. 2022), to globular clusters, which have long since halted any star formation (Kirsten et al. 2022), although this may be biased towards the repeating subset of the population, which allow VLBI follow-up. This suggests multiple pathways capable of producing FRB progenitors, each of which favours different astrophysical environments, and hence different classes of FRB host galaxies. Therefore, the cosmological evolution of the FRB population (and hence their host galaxies) may be complex, with some FRBs tracing star formation with a cosmologically insignificant delay of tens of millions of years, and potentially favouring low-metallicity environments; while others may result from long-duration mergers and may better correlate with the total stellar mass of their host. Untangling such complexity is important both for studies of FRB host galaxies, and those that fit the redshift-dispersion measure distribution of the FRB population. In this work, we focus on the former, but note that these results are critical for the latter.

Several works have analysed FRB host galaxies and compared their properties to those of field galaxies, with a picture gradually emerging of the hosts of apparently once-off FRBs approximately tracing the star-forming main sequence (Gordon et al. 2023), sharing similar properties to the hosts of core-collapse supernovae (CCSNe) and short-duration gamma-ray bursts (sGRBs) (Bhandari et al. 2022). However, it has been observed that there is a deficit of low-mass dwarf hosts with high star-formation rates (SFRs) (Bhandari et al. 2020; Heintz et al. 2020), especially when compared to the host galaxies of long-duration gamma-ray bursts (LGRBs) and superluminous supernovae (SLSNe) (Bhandari et al. 2022), which has been attributed to the FRB progenitors favouring higher metallicity environments (Sharma et al. 2024), although this is debated (Loudas et al. 2025; Yamasaki et al. 2026). Horowicz & Margalit (2026) argue that FRB hosts appear to trace a linear combination of stellar mass and SFR (those authors also consider, and rule out, globular clusters); however, as noted by Loudas et al. (2025), there appears to be an excess of dwarf FRB host galaxies with relatively low SFR, which cannot be explained by either model. Furthermore, the sub-class of highly active FRBs

Corresponding author: Clancy W. James; Email: clancy.james@curtin.edu.au

Cite this article: James CW, Loudas N, Woodland M, Andersen BC, Prochaska X, Hoffmann JL, Marnoch L and Ryder S. (2026) Updating the PATH framework with FRB host galaxy models. *Publications of the Astronomical Society of Australia* **43**, e109, 1–15. https://doi.org/10.1017/pasa.2026.10224

© The Author(s), 2026. Published by Cambridge University Press on behalf of Astronomical Society of Australia. This is an Open Access article, distributed under the terms of the Creative Commons Attribution licence (https://creativecommons.org/licenses/by/4.0/), which permits unrestricted re-use, distribution and reproduction, provided the original article is properly cited.

associated with PRSs do appear to come from dwarf, star-forming hosts (e.g. Moroianu et al. 2026), with PRS properties that may be evolving on year-long timescales, suggesting an origin in a young supernova remnant (Niu et al. 2026), and giving further evidence to a correlation with massive star formation.

All the above results rely on confident associations of FRBs with their (nominal) host galaxies. The standard methodology has been the implementation of the Probabilistic Association of Transients to their Hosts (PATH; Aggarwal et al. 2021), a Bayesian framework that associates candidate host galaxies identified in optical images with FRB localisations from radio telescopes. PATH integrates priors on the FRB host galaxy magnitude and offset distribution to assign posterior probabilities of each galaxy being the true host, or the true host being unseen in the image. PATH has been applied to determine the hosts of FRBs detected with the Australian SKA Pathfinder (ASKAP; Shannon et al. 2025), the MeerKAT telescope (Pastor-Marazuela et al. 2026), the Deep Synoptic Array (DSA; Sharma et al. 2024), and the Canadian Hydrogen Intensity Mapping Experiment (CHIME; CHIME/FRB Collaboration et al. 2025).

The current application of PATH to the FRB literature has suffered two main critiques. The first is that, like any Bayesian framework, the posterior probabilities assigned by PATH are a function of the assumed prior distributions, and these were developed at a time when little was known about FRB hosts. However, this is no longer the case. In particular, the relationship between FRB dispersion measure (DM) and host galaxy redshift (z), known as the 'Macquart relation' (Macquart et al. 2020), is now well-studied. Several works modelling the FRB z–DM relation have been developed (Gardenier et al. 2019; James et al. 2022; Shin et al. 2023), all of which can model the probability distribution of an FRB's redshift from its DM, $P(z|\mathrm{DM})$. In particular, an FRB's DM places a stringent upper limit on its distance, since while over-dense structures in the Universe (e.g. galaxies, galaxy groups, halos, and filaments) can readily produce an excess of DM, nothing produces a negative DM, and even voids have a certain minimum density (James et al. 2022; Sharma et al. 2026). In theory therefore, and almost uniquely among different classes of astrophysical transients, an FRB's DM can be used to inform prior probabilities on its host distance, and hence apparent magnitude. A consequence of this is that a low-DM FRB is much more likely to have a detectable host galaxy than a high-DM FRB, and this should be reflected in the prior probability of an FRB's true host galaxy being visible in an optical image. Similarly, the probability of seeing the true host should reflect the depth of the optical image being used to search for it. For example, one might imagine that the prior on the true host galaxy being unseen in an image should be much lower for an FRB with a DM of 100 pc cm^{-3} studied with the Hubble Space Telescope than it should be for a 3 500 pc cm^{-3} FRB searched-for in ground-based archival data.

Quantifying the effects of optical follow-up depth, and the predictive power of an FRB's DM, requires a model for FRB host galaxies that can turn a redshift prediction, $P(z|\mathrm{DM})$, into a prediction for observable galaxy properties – for instance, via a prediction for r-band magnitude, $P(m_r|z)$. While such a model might usefully predict many other galaxy properties (star-formation history, metallicity, etc.), we focus on magnitude only. This is most relevant because PATH is typically used to select a likely host from a single photometric observation, with more-detailed optical follow-up observations subsequently yielding further data. Despite the many aforementioned works analysing the specific properties of FRB hosts however, relatively few (e.g. Marnoch et al. 2023; Loudas et al. 2025; Horowicz & Margalit 2026) have developed specific models of FRB hosts with which to compare to data. Ideally, developing such a model would not only enable the use of an FRB's DM to create informed priors for host identification with PATH, it would also allow model parameters to be fit to the subsequent FRB host distribution, providing information on the progenitors of FRBs.

The second critique relates to the interpretation of PATH output, in particular the tendency to separate host galaxy candidates into 'firm' hosts if their posterior probability of being the true host is greater than, for example, 90% and to discard hosts lower than this threshold. However, any Bayesian framework can only produce an unbiased posterior distribution when summing over all outcomes – in this case, candidate host galaxy properties – weighted by their posterior probabilities. This has recently been demonstrated in the case of PATH by B. C. Andersen et al. (in preparation). While we cannot correct for this bias in this work, since doing so would require spectroscopic observations of a large number of FRB host candidates, we consider it important to estimate the degree of bias in the current literature produced by this approximation.

We first therefore review and expand the PATH framework in Section 2, before developing models of the FRB host galaxy apparent magnitude distribution as a function of redshift $P(m_r|z)$ in Section 3. In Section 4, we combine these with estimates of FRB redshift, $P(z|\mathrm{DM})$ and fit these models to optical follow-up observations of 32 FRBs observed with ASKAP in incoherent sum (ICS) mode by CRAFT. We present our fit results, together with updated estimates of the intrinsic FRB host galaxy distribution, and probabilities for galaxies being the true host, in Section 5. Finally, in Section 6, we discuss the implications of our results.

2. PATH, revisited

In this Section, we briefly recap the standard PATH framework (a more comprehensive review can be found in B. C. Andersen et al. in preparation), before presenting our updates to the methodology. We first show how priors on host galaxy magnitudes can be incorporated into the standard PATH framework, before revisiting the calculation of PATH posteriors and concluding with a final note on the correct normalisation of candidate priors. In this Section, we use a generic m to indicate an apparent magnitude in an arbitrary band; later, we will specifically use r-band magnitudes m_r. However, we note that, by replacing m, the below analysis could readily be applied to any other host property. Throughout, we refer readers to Table 1, to track both original PATH notation, and new notation introduced here.

2.1. Recap of the original PATH framework

The PATH framework uses two sets of priors. One is on the radial offset distribution with respect to the centre of the true host, $P(\omega)$. This is typically modelled as an exponential in terms of the host galaxy's angular size, ϕ, and weighted by a factor $2\pi\omega$ to account for the greater solid angle at larger radii. Recent data prefer a scale length of $\phi/2$ (Shannon et al. 2025). This work however focuses on the second prior, $P(O_i)$, giving the probability of a particular galaxy O_i being the true host given its apparent magnitude, m.

https://doi.org/10.1017/pasa.2026.10224 Published online by Cambridge University Press

Table 1. PATH notation used in this work. The upper portion summarises notation from the original PATH work of Aggarwal et al. (2021); the lower portion, new notation introduced here.

Original PATH terminology		
Symbol	Unit	Description
m	mag	Apparent magnitude
m_r	mag	Apparent r-band magnitude
Σm_i	Gal arcsec^{-2}	Cumulative density of galaxies with magnitude $m < m_i$ on the sky
x	deg	Radio localisation position (RA,DEC) of an FRB on the sky
ϕ	arcsec	Galaxy half-light radius
θ	arcsec	Observed offset between FRB and host candidate centre
ω	arcsec	True offset between FRB and its host
O_i		The ith host galaxy candidate
$P(O_i)$		Prior of host galaxy candidate i being the true host
$P(x\|O_i)$		Probability of observing FRB position $\vec{x}$ given that host candidate O_i is the true host
$P(O_i\|x)$		Posterior probability of host galaxy candidate i being the true host, given FRB localisation x
$P(U)$		Prior of the true host galaxy being unidentified in an image
$P(U\|x)$		Posterior probability of the true host galaxy candidate being unidentified in an image, given FRB localisation x
Updated terminology from this work		
Symbol	Unit	Description
$\rho_{D16}(m)$	Gal arcsec^{-2} mag^{-1}	Intrinsic angular density of galaxies with magnitude m on the sky, taken from Driver et al. (2016)
$\rho(m)$	Gal arcsec^{-2} mag^{-1}	Apparent angular density of galaxies with magnitude m on the sky, as identified by an optical system
Ω	arcsec^2	Angular size of optical image about FRB position
N_O		Number of host galaxy candidates
$\mathbf{x}$		Set of positions of all FRB host galaxy candidates in an image, relative to the FRB localisation $\vec{x}$
$P(\mathbf{x}, N_O)$		Probability of observing a set of N_O host galaxy candidates with positions $\mathbf{x}$
$P(\mathbf{x}, N_O\|O_i)$		Probability of observing a set of N_O host galaxy candidates with positions $\mathbf{x}$ given that O_i is the true host
$P(O_i\|\mathbf{x}, N_O)$		Posterior probability of the true host being galaxy O_i given N_O host galaxy candidates with positions $\mathbf{x}$
$P(\mathbf{x}, N_O\|U)$		Probability of observing a set of N_O host galaxy candidates with positions $\mathbf{x}$ given that the true host is unseen
$P(U\|\mathbf{x}, N_O)$		Posterior probability of the true host being unseen given N_O host galaxy candidates with positions $\mathbf{x}$

The standard host prior is the 'inverse' prior,

$$P(O_i) = \frac{1}{\Sigma m_i}, \tag{1}$$

where Σm_i is the angular number density of galaxies with magnitude $m \leq m_i$ on the sky, taken from Driver et al. (2016). A prior on the true host being unobserved, $P(U)$, is defined, and the priors $P(O_i)$ get re-normalised to ensure that

$$\sum_i P(O_i) = 1 - P(U). \tag{2}$$

Given these priors, PATH calculates Bayesian posteriors according to

$$P(O_i|x) = \frac{P(x|O_i)P(O_i)}{P(x)}, \tag{3}$$

$$P(U|x) = \frac{P(x|U)P(U)}{P(x)}, \tag{4}$$

where x represents the observable information, that is, the FRB localisation relative to galaxies identified in the optical image. The term $P(x|O_i)$ accounts for the offset prior $P(\omega)$, the FRB localisation ellipse, and the position and size of host candidate i with respect to that localisation. As we do not address this factor in this work, we refer readers to Aggarwal et al. (2021) for further details of its calculation. The factor $P(x|U)$ is simply set to Ω^{-1}, that is, the inverse size of the optical image, Ω. Thus the normalising factor $P(x)$ is calculated as

$$P(x) = P(x|U)P(U) + \sum_i P(x|O_i)P(O_i). \tag{5}$$

2.2. Re-evaluating the probability of an observation within PATH

Here, we derive a new formula for the probability of an observation, which affects how PATH posteriors are calculated. We ignore galaxy clustering in our derivation and treat all galaxy observations as independent. We comment on this assumption below. We first note that the 'observation', in a Bayesian sense, includes both the radio localisation information from the FRB detection, relative to the locations of candidate galaxies, and the existence of N_O host candidates in the analysed image area Ω. Here, we explicitly separate these terms, and instead of using the FRB localisation x, we define $\mathbf{x}$ to be the set of positions of host candidates relative to the FRB localisation x, while N_O refers to the number of candidates, for reasons that will become apparent later. All probabilities in this Section are functions of candidate host magnitudes, so we

https://doi.org/10.1017/pasa.2026.10224 Published online by Cambridge University Press

do not explicitly write this dependence in the equations. The usual normalisation applies, being that the probability of this observation is equal to the sum of the probabilities that each individual galaxy is the true host, plus the probability that none of them are the true host, that is,

$$P(\mathbf{x}, N_O) = \sum_i P(\mathbf{x}, N_O|O_i)P(O_i) + P(\mathbf{x}, N_O|U)P(U), \quad (6)$$

where $P(\mathbf{x}, N_O|O_i)$ is the probability of the observation given that galaxy O_i is the true host, and $P(\mathbf{x}, N_O|U)$ is the probability of that observation given that the true host is unobserved. These disjoint scenarios are weighted against the usual priors, $P(O_i)$ and $P(U)$.

The term $P(\mathbf{x}, N_O|O_i)$ includes the standard term $P(\mathbf{x}|O_i)$ from PATH; however, if O_i is the true host, the presence of all other galaxies must be coincidental (in the regime where galaxy clustering is ignored). Thus we find

$$P(\mathbf{x}, N_O|O_i) = P(\mathbf{x}|O_i)\,\Pi_{j=1,j\neq i}^{N_O}\rho(m_j), \quad (7)$$

where $\rho(m_j)$ is the angular number density on the sky of all galaxies having magnitude m_j, that is, it is the derivative of Σm_j. Since all $j \neq i$ galaxies are not the true host, their positions in the image with respect to $\mathbf{x}$ hold no information and thus have a uniform probability density of $P(\mathbf{x}) = \Omega^{-1}$, where Ω is the analysed image area; however, the probability of that galaxy being present in the image is $\Omega\rho(m_j)$, so that these factors of Ω cancel. Given that O_i is the host, its presence is guaranteed, so the probability of it being in the image is unity.

Similarly, given that the true host is unseen, the probability of seeing that configuration of galaxies is

$$P(\mathbf{x}, N_O|U) = \Pi_{j=1}^{N_O}\rho(m_j), \quad (8)$$

since the presence of each must be coincidental. We can now write Equation (6) as

$$\begin{aligned} P(\mathbf{x}, N_O) &= \sum_i \left(P(\mathbf{x}|O_i)\,\Pi_{j=1,j\neq i}^{N_O}\rho(m_j)\right) P(O_i) \\ &\quad + \Pi_{j=1}^{N_O}\rho(m_j)P(U) \\ &= \Pi_{j=1}^{N_O}\rho(m_j)\left[\sum_i \frac{P(\mathbf{x}|O_i)P(O_i)}{\rho(m_i)} + P(U)\right]. \end{aligned} \quad (9)$$

Comparing Equation (9) to the standard PATH framework, we observe firstly that the leading normalising constant is the probability of all galaxies being present in such an image irrespective of the FRB host considerations. It can therefore be ignored entirely in the calculation of posteriors, and for likelihood maximisation purposes, since it is a common factor in all calculations. Next, we see that the term $P(\mathbf{x}|O_i)P(O_i)\rho(m_i)^{-1}$ is almost identical to Equation (3), except for the replacement of Σm_i with its derivative, $\rho(m_i)$. Lastly, we note that the prior $P(U)$ appears in unmodified form. Effectively, this implies that $P(\mathbf{x}|U) = 1$, that is, that these foreground galaxies were always going to exist irrespective of the FRB localisation.

Removing therefore the common leading factor from Equations (7)–(9) gives

$$P(\mathbf{x}, N_O) = \sum_i \frac{P(\mathbf{x}|O_i)P(O_i)}{\rho(m_i)} + P(U), \quad (10)$$

$$P(U|\mathbf{x}, N_O) = \frac{P(U)}{P(\mathbf{x}, N_O)}, \quad (11)$$

$$P(O_i|\mathbf{x}, N_O) = \frac{P(\mathbf{x}|O_i)P(O_i)}{P(\mathbf{x}, N_O)\rho(m_i)}. \quad (12)$$

2.3. A comment on PATH prior normalisation

A key (and fairly obvious) identity should hold in all stages of a PATH analysis: that the probabilities of the host being seen, and unseen, should sum to unity. In the original PATH work, this is applied via Equation (4) of Aggarwal et al. (2021), which we have written as Equation (2). However, writing this equation in this manner misses one key subtlety which only becomes obvious when constructing priors based on host galaxy magnitudes. This is that priors should be set before looking at an image; once a list of candidate hosts O_i have been identified in an image, any priors should be updated to reflect that observation (i.e. they are not 'priors' anymore)! This becomes critical once expectations for FRB host galaxy properties are set: if one expects FRB hosts to be bright and star-forming, but only a red-and-dead dwarf galaxy is observed in an image, then a reasonable observer would increase their expectation of the true host being unobserved. However, within the original PATH framework, the sum of priors on all observed galaxies gets renormalised to $1 - P(U)$ via Equation (2). Thus an optical image with a single unlikely host candidate would have that candidate's prior renormalised to $1 - P(U)$, as would an optical image with a single likely host candidate.

As it turns out, this distinction did not matter for the original PATH analysis, since the priors $P(U)$ were by construction rather generic and not based on any particular expectation of the nature of the FRB host galaxy. In that sense, this behaviour was a feature, rather than a bug, and ensured that the DM–z relation found by Macquart et al. (2020) was not influenced by such priors. Indeed, a generic prior of, for example, $P(U) = 10\%$ could not be updated once a list of candidates O_i was found in an image, because there was no framework to determine if, having observed those candidates, $P(U)$ should become more or less likely. However, for this work, this distinction now becomes critical.

Here, we construct priors $P(m)$, which is the probability that the true host has apparent magnitude m. We ensure that our prior expectations are correctly normalised by requiring that

$$\int P(m)dm = 1. \quad (13)$$

We also construct a function $P(O|m)$ in Section 4.1, such that

$$P(O) = \int P(O|m)P(m)dm \quad (14)$$

$$P(U) = \int (1 - P(O|m))P(m)dm, \quad (15)$$

which ensures correct normalisations on the priors that the true host is or is not seen in an image. The prior $P(O_i)$ that a particular galaxy of magnitude m_i is the host is therefore the integrand of Equation (14), that is,

$$P(O_i) = P(O|m_i)P(m_i). \quad (16)$$

This effect must also be accounted for in the galaxy density function, $\rho(m_i)$. Thus we use

$$\rho(m_i) = P(O|m_i)\rho_{\rm D16}(m_i) \quad (17)$$

where $\rho_{\rm D16}(m_i)$ is the galaxy density function from Driver et al. (2016). In effect, this means that factors $P(O|m_i)$ in both the

https://doi.org/10.1017/pasa.2026.10224 Published online by Cambridge University Press

numerator and denominator of Equation (10) cancel, and this term affects the likelihood only through $P(U)$ – which then indirectly affects $P(O_i|\mathbf{x}, N_O)$ in Equation (12).

Out of curiosity, we derive an updated version of Equation (2), that is, a set of updated priors once FRB host galaxies are seen in an image, but before positional information is included. This is accomplished by removing all positional information from Equation (9), obtaining

$$P(N_O) = \Pi_{j=1}^{N_O} \Omega\rho(m_j) \left[\sum_i \frac{P(O_i)}{\Omega\rho(m_i)} + P(U) \right], \tag{18}$$

$$P(O_i|N_O) = \frac{1}{P(N_O)} \sum_i \frac{P(O_i)}{\Omega\rho(m_i)}, \tag{19}$$

$$P(U|N_O) = \frac{P(U)}{P(N_O)}, \tag{20}$$

where the factors Ω have re-entered the equation, since they are no longer cancelled by $P(\mathbf{x}) = \Omega^{-1}$ for galaxies which are not the host. In an extreme case, where the Ω is extremely small, the presence of even a single galaxy will make that the likely host. Conversely, when Ω is extremely large, the summation over individual O_i becomes an integral over the observable galaxy magnitude distribution $P(m)$, with a density equal to the expected background density

$$\begin{aligned} \sum_i \frac{P(O_i)}{\Omega\rho(m_i)} &\Rightarrow \frac{1}{\Omega} \int \frac{n(m)P(O|m)P(m)}{\rho(m)} dm \\ &\sim \frac{1}{\Omega} \int \frac{\Omega\rho(m)P(O|m)P(m)}{\rho(m)} dm \qquad (21) \\ &= \int P(O|m)P(m)dm \\ &= P(O), \qquad (22) \end{aligned}$$

and thus the priors will not be updated, as might be expected.

2.4. Qualitative effects of clustering

We finally comment on the qualitative effects of galaxy clustering. Firstly, our priors $P(U)$ and $P(O_i)$ will be unaffected by clustering, since whether or not the true host is visible in an image is determined only by the properties of the host. It will however affect the calculation of posterior probabilities. Yet, the effect may be small, as can be demonstrated with this trivial example. Consider a Universe with all galaxies having equal magnitude, and a galaxy density of one per ten square arcseconds ($\rho = 0.1$). However, galaxies are clustered such that one in every hundred square arcseconds has ten galaxies, that is, $\rho_{\rm cluster} = 0.01$. Observing a cluster of $N_O = 10$ galaxies in an optical image of 1″ about an FRB localisation should therefore increase the posterior of observing the true host, $P(O|N_O)$, by the inverse of the cluster density, $\rho_{\rm cluster}^{-1} = 100$, relative to $P(U|N_O)$, since if the true host (and hence, the host cluster) is unobserved, there is a 1% chance of coincidentally observing a cluster along that line of sight. If instead we ignore clustering and use Equation (18), each individual galaxy in the cluster will have the posterior updated by a factor of $\rho^{-1} = 10$. Yet this will be summed over all ten cluster galaxies, yielding the correct factor of 100. Whether or not such equality holds for non-trivial examples remains an open question. However, this does suggest that ignoring clustering will not significantly skew our posterior calculations.

3. Host galaxy models

Galaxies are complex. Within the context of FRB research, their primary observables are their apparent magnitude and angular extent, by which they are assessed as host galaxy candidates by PATH as discussed above; and their redshift, which allows them to be placed on the z–DM relation. However, a whole host of properties can be extracted from spectroscopic observations, such as stellar mass, SFR, metallicity, and star-formation history (e.g. Gordon et al. 2023), while radio observations inform us of HI and continuum emission (Glowacki et al. 2024).

In this initial work, we aim to model only a function $P(m_r|z)$, giving the distribution of apparent r-band magnitudes m_r as a function of redshift. This is because most efforts to identify FRB hosts rely only on a single observation, typically with an r-band filter (here, we approximate R-band and r-band filters as being identical, and use 'r' to refer to both). We develop three different models and then compare their predictions against observations of FRBs with ASKAP.

3.1. Model 1: Empirical ('Marnoch23')

Our empirical model (which we refer to as the 'Marnoch23' model) is that presented by James et al. (2026) based on the work of Marnoch et al. (2023), who derive the $m_r(z)$ curves for 23 FRB host galaxies. The model uses a Gaussian, with redshift-dependent parameters, to characterise the $m_r(z)$ distribution, with mean $\mu(z)$ and standard deviation $\sigma(z)$ fit to the mean and RMS of the curves derived by Marnoch et al. (2023). The key advantage of this model is that no assumptions about the FRB host galaxy distribution need to be made. Rather, it just uses the available information for actual FRB hosts, accounting for all their complexity, irrespective of whether or not we as astronomers understand it. It also naturally includes K_r-corrections for each host individually, since the spectra were fit with PROSPECTOR (Leja et al. 2017). However, the model does not account for the evolution of galaxies: FRB hosts may look quite different at $z = 1$ to those at $z = 0$, and this sample all had hosts within $z < 0.5$. Furthermore, while 17 of the FRB hosts used in the model were localised by the CRAFT collaboration and represented a mostly complete sample (with the exception of the FRB in question, FRB 20210912A, which at time of publication did not have any known host Marnoch et al. 2023) it also included six others of mixed provenance, for example, FRB 20190520B, which was localised only because it is a strong repeater (Niu et al. 2022). Finally, the model is based on 'firm' hosts, and thus is subject to all the biases that we discuss in Section 1 – indeed, it was developed precisely because the host of FRB 20210912A was too faint to be visible in optical and near-infrared follow-up observations. We also note that the model is completely specified: there are no free parameters which would allow the model to be adjusted or fit to further data, for example, to hosts too faint to be included in the original sample of 23 FRBs.

3.2. Model 2: Predictive ('Loudas25')

Our second model is based on GALFRB,[a] a package developed by Loudas et al. (2025) to generate galaxy populations that trace

[a] github.com/loudasnick/GALFRB.

https://doi.org/10.1017/pasa.2026.10224 Published online by Cambridge University Press

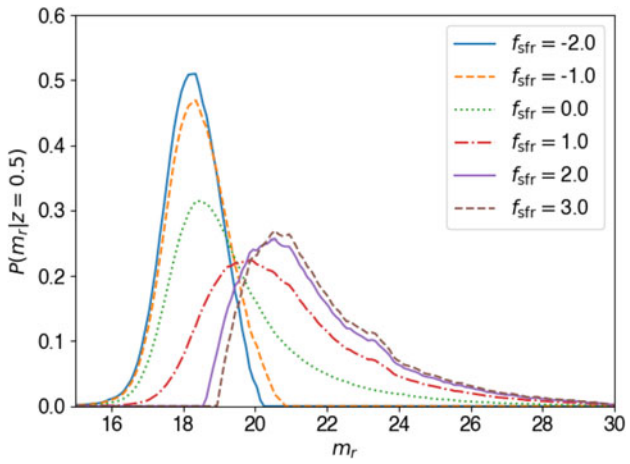


Figure 1. Probability distributions $P(m_r|z)$ at $z = 0.5$ for various values of f_{sfr} using the Loudas25 model.

various physical quantities, such as SFR and/or M^*, while accounting for redshift evolution. GALFRB is built on the probability density function $\rho(\mathrm{SFR}, M^*, z)$, given by the trained neural network (NN) presented by Leja et al. (2022), and is based on data from the COSMOS-2015 (Laigle et al. 2016) and 3D-HST (Skelton et al. 2014) UV-IR catalogues in the redshift range 0.2–3. GALFRB incorporates analytical expressions to complete the model in the low-z, low-M^* range, where data are insufficient to train the NN. The r-band magnitudes are sampled for each galaxy by modelling the full rest-frame mass-to-light ratio distribution via the $g - r$ colour which in turn depends on SFR; these values are then K_r-corrected according to Kim et al. (2023), yielding apparent magnitude values. We refer readers to Loudas et al. (2025), and references contained therein, for further details of the modelling.

We generate redshift-dependent magnitude distributions, $P(m_r|z)$, by sampling mock galaxies in a redshift grid with resolution $\Delta z = 0.01$ from 0.01-2. Selecting galaxies weighted by their stellar mass M^* produces $P_{M^*}(m_r|z)$, while weighting by their SFR produces $P_{\mathrm{SFR}}(m_r|z)$. We smoothly scale between these scenarios by using the factor f_{sfr}, producing

$$P(m_r|z) = f_{\mathrm{sfr}} P_{\mathrm{SFR}}(m_r|z) + (1 - f_{\mathrm{sfr}}) P_{M^*}(m_r|z). \quad (23)$$

Probabilities at redshifts less than $z = 0.01$, and greater than $z = 2$, were extrapolated by scaling and shifting the distribution corresponding to the lowest/highest redshift bin according to the relative luminosity distance only. Example distributions of $P(m_r|z)$ are given in Figure 1. The M^*-weighted distribution ($f_{\mathrm{sfr}} = 0.0$) predicts brighter hosts than the SFR weighted distribution ($f_{\mathrm{sfr}} = 1.0$); thus, higher f_{sfr} values yield fainter galaxy populations. Extrapolating the distributions to very low ($f_{\mathrm{sfr}} < -2$) or very high ($f_{\mathrm{sfr}} > 3$) values produces little change in the predictions, so we only consider the range $-2 \leq f_{\mathrm{sfr}} \leq 3$ in this work.

This model has several advantages. First, it is based on a large sample of galaxies and thus accounts for redshift evolution of the galaxy population. Its direct dependence on SFR and M^* allows us to test predictions for FRB host galaxies in a manner that informs us about FRB origins. Consistency with $f_{\mathrm{sfr}} = 1$ would clearly indicate that FRBs trace star-formation, and may originate in CCSNe; while $f_{\mathrm{sfr}} = 0$ would perhaps indicate a merger origin with a very large lag compared to star formation. An intermediate value may indicate a mixed population. Even though f_{sfr} has a physical meaning only in the range $0 \leq f_{\mathrm{sfr}} \leq 1$, we relaxed this condition by numerically allowing for unphysical values of $f_{\mathrm{sfr}} > 1$ and $f_{\mathrm{sfr}} < 0$, by setting $P(m_r|z)$ to zero if it would otherwise become negative, although the interpretation of such values is unclear. See Section 6 for further discussion of such scenarios, in light of our results.

A potential disadvantage of the model is that FRB hosts can only be sampled according to M^* and SFR, so that effects such as metallicity, moderate time-delays with respect to star formation, or other galaxy properties that may influence FRB creation cannot be explicitly accounted for. We note that metallicity could in principle be incorporated, as it is a function of SFR and $M^\star$ (Yamasaki et al. 2026), but we leave this to a future work.

3.3. Model 3: Naive (this work)

Our final model is termed the 'Naive' model, because it is not based on any astronomical observations. Rather, it models FRB hosts as having a fixed distribution in absolute magnitude M_r, which is then scaled to apparent magnitude m_r using only the luminosity distance, and a K-correction-like term. We parameterise the M_r distribution using six values between $M_r = -25$ and $M_r = -15$ and use linear interpolation to infer the full $P(M_r)$ distribution (see Appendix 1 for a justification of this choice). We include a simple redshift dependence which acts both as a K_r-correction and evolutionary correction, so that

$$m_r = M_r + 5 \log_{10} L_d - 5 - K_r \quad (24)$$

where the redshift dependence is encapsulated in the nominal K-correction

$$K_r = 2.5k \log_{10} (1 + z). \quad (25)$$

In reality, the redshift dependence will be much more complicated: galaxy evolution will affect the distribution $P(M_r)$ through various processes, introducing a complex z-dependence, and the actual K_r-correction will also be more complex. For now, we instead introduce only a single term, and test for the significance of $k \neq 0$ in our fits.

The advantage of this model is that it is generic – there are no prior assumptions about FRB astrophysics, and it therefore cannot be influenced by any of the biases discussed in this work. The disadvantages of the model are obvious: it can only account for galaxy evolution and spectra via a single K_r-correction term applied to the model as a whole, which vastly over-simplifies the complexities of the galaxy population. Furthermore, it will be difficult to relate model results to astrophysical conclusions about FRB origins.

4. Evaluation

4.1. Dataset, and P(O|m)

We use optical follow-up images for 32 of the ASKAP/CRAFT ICS survey FRBs (Shannon et al. 2025), which were centred on the FRB radio localisations. This includes all available data from this sample, with the exceptions of FRB20230731A and FRB20230718A, which lie within the Galactic plane. The images were taken with the FOcal Reducer and low dispersion Spectrograph (FORS2; Appenzeller & Rupprecht 1992) on the ESO Very Large Telescope (VLT), and processed as described in Marnoch et al. (2023). Approximately half the targets were observed in the R-band, with the remainder in g and I band. We convert these latter data to the R-band as described in Section 4.2.

https://doi.org/10.1017/pasa.2026.10224 Published online by Cambridge University Press

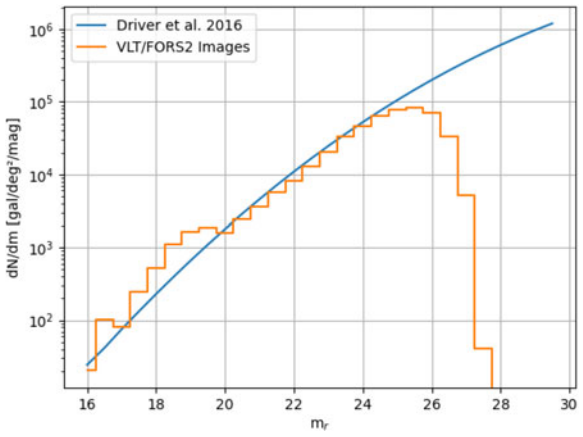


Figure 2. Galaxy number density per magnitude bin identified in images about the nominal positions of CRAFT/ICS FRBs. Also shown are the galaxy densities from Driver et al. (2016).

Galaxies are identified in each optical image using SExtractor (Bertin et al. 2020; Kümmel et al. 2020), with DE - TECT_MINAREA = 5 and DETECT_THRESH = 1.5. Only galaxies identified within a 1′ cutout of the FRB source are considered as plausible hosts (the largest localisation uncertainty for the sample is ≈ 2″ for FRB 20190711A) and kept for further analysis.

Figure 2 shows the distribution of optical magnitudes of all FRB host candidates in these images, plotted against the *r*-band density function from Driver et al. (2016). It is evident that, compared to expectations from field galaxies, the observations become incomplete beyond magnitude $m_r = 25$, with the dimmest identifiable galaxy being at $m_r = 27$. The excess of galaxies in the $18 \leq m_r \leq 20$ range is due to mis-classified stars. We remove these by hand if they occur in the vicinity of the FRB, but we have not done this over the entirety of all images. They thus represent a small contamination to Figure 2, which we estimate to be negligible for purposes of estimating completeness.

We next introduce the last piece of our framework, which calculates the probability that a galaxy of magnitude m_r is identified in a given optical image, that is, $P(O|m_r)$. To estimate this, we use a procedure similar to that of B. C. Andersen et al. (in preparation). We use SExtractor to extract sources from the VLT/FORS2 images and exclude any source from our sample with CLASS_STAR > 0.8. In addition, any object with a magnitude $m > 23$ is classified as a galaxy. We then construct the observed angular density function $\rho_{\mathrm{VLT/FORS2}}(m_r)$, and calculate the ratio between this and the expected number density $\rho(m_r)$ from Driver et al. (2016). A small scaling factor is applied so that the completeness of each is equal at bright magnitudes. The resulting ratio is shown in Figure 3, together with equivalent data from the Panoramic Survey Telescope and Rapid Response System Survey (Pan-STARRS; Chambers et al. 2016) and the DESI Legacy Imaging Surveys (hereafter the Legacy Surveys; Dey et al. 2019) taken from B. C. Andersen et al. (in preparation). We parameterise this distribution with the expression

$$P(O|m_r) = \frac{1}{1 + \exp\left[(\mu_m - m_r)/\sigma_m\right]} \tag{26}$$

which provides a good fit to both data from B. C. Andersen et al. (in preparation) and VLT/FORS2. The best-fit values are reported in Table 2.

Table 2. Fits of Equation (26) to data from B. C. Andersen et al. (in preparation) and FORS2 data from this work.

Optical data	μ_m	σ_m
VLT/FORS2	26.2	0.34
Legacy surveys	24	0.55
Pan-STARRS	21.8	0.54

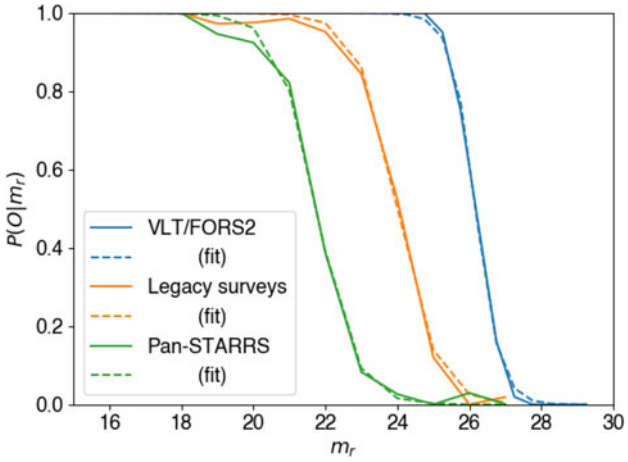


Figure 3. Data and fits to the probability $P(O|m_r)$ of a galaxy being identified in optical images given its *r*-band magnitude, m_r. Data for the Legacy Surveys and Pan-STARRS from B. C. Andersen et al. (in preparation); FORS2 from this work. Fits according to Equation (26) with parameters from Table 2.

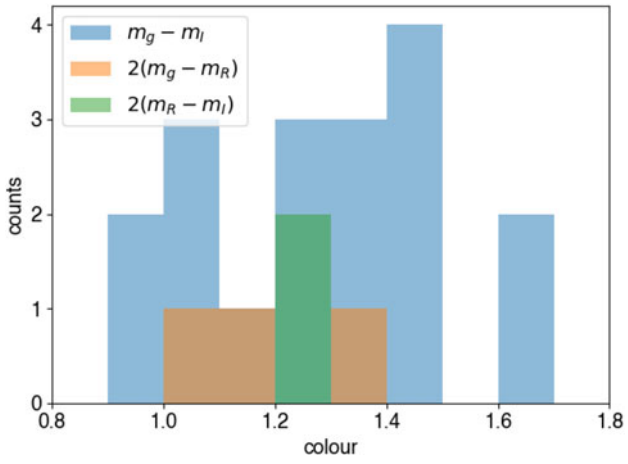


Figure 4. Histograms of VLT/FORS2 colours for ASKAP/ICS FRB hosts identified by Shannon et al. (2025).

4.2. Colour correction

The VLT/FORS2 photometry used in this work was taken predominantly in either *g* and *I* bands, or *R* band. Figure 4 shows $g - I$ colours for the 18 ICS FRBs with data taken in both bands, for the most likely FRB hosts identified by Shannon et al. (2025). It also shows $R - I$ and $g - R$ colours for the 2 and 4 FRBs with data in both of those respective bands, multiplied by two to account for these bands being closer together than $g - I$, for visualisation purposes. The mean $g - I$ colour for the sample is 1.3, with the $R - I$ and $g - R$ colours having means of 0.6 and 0.7, respectively.

https://doi.org/10.1017/pasa.2026.10224 Published online by Cambridge University Press

Galaxy surveys reveal a bimodal distribution in colour, due to the star-forming and quenched populations, with green valley galaxies in-between (Blanton et al. 2003). FRB hosts tend to follow the star-forming main-sequence, with a small fraction transitioning to quiescence (Gordon et al. 2023). This explains the relatively small variance in observed $m_r - m_I$ and $m_g - m_R$; however, our small sample sizes are inadequate to fully capture the variance. When running our PATH analysis therefore, we assume constant corrections of $m_g - m_R = 0.65$ and $m_R - m_I = 0.65$ and use these to convert galaxy magnitudes from the g-band and I-band images to their R-band equivalents. We estimate that this leads to errors of ~ 0.3 on m_r.

4.3. Procedure for estimating P(z)

The extragalactic DM distribution of FRBs has been shown to correlate with their redshift. This was first indicated by Shannon et al. (2018), who showed that the brighter (and therefore, likely closer) FRBs had lower DMs, and then most famously by Macquart et al. (2020), who proved that the DMs of FRBs increase with their redshift according to the expected baryonic density of the Universe. Many works have since attempted fits of the z–DM relationship, which (when done properly) include estimates of the detection bias against higher DMs, the FRB luminosity function and source evolution, as well as accounting for fluctuations in the density of ionised gas (Connor 2019; Luo et al. 2020; Shin et al. 2023). Nonetheless, estimates for the FRB z–DM distribution remain model-dependent, with choices such as the functional form of the luminosity function, source evolution, or frequency dependence of FRBs affecting the conclusions drawn about the population (Hoffmann et al. 2025). Of specific note here is that these estimates are typically based upon identified FRB host galaxies, the validity of which we explicitly set out to test in this work. In the future, we aim to simultaneously incorporate completeness in FRB hosts into FRB population and cosmological parameter fitting.

In this work, we use the zDM code of James et al. (2022) to predict the $P(z|\mathrm{DM_{EG}})$ distribution for each FRB. The extragalactic contribution to the DM budget, $\mathrm{DM_{EG}}$, is calculated by subtracting local contributions from the Milky Way's interstellar medium (estimated using the NE2001 model of Cordes & Lazio 2003) and an assumed halo contribution of 68 pc cm^{-3} (Hoffmann et al. 2026) from the FRB's measured DM. In the near future, we plan to update zDM to the NE2025 model (Ocker & Cordes 2026). However, this has not yet been implemented within zDM.

We assume standard Planck cosmology (Planck Collaboration et al. 2016) and take FRB parameters such as the luminosity function and population evolution from Hoffmann et al. (2026). This is exactly the same procedure as we use in James et al. (2026) to calculate predictions for Vera C. Rubin's Legacy Survey of Space and Time using the Marnoch23 model.

For each of three characteristic ASKAP/ICS central frequencies (900, 1 300, and 1 600 MHz) therefore, we create best-fitting z–DM grids as per James et al. (2022), which produces predictions for $P(z|\mathrm{DM_{EG}})$. Our priors thus become

$$P(O_i) = \int P(O|m_i)\, P(m_i|z)\, P(z|\mathrm{DM_{EG}}) dz, \tag{27}$$

$$P(U) = \iint [1 - P(O|m_r)]\; P(m_r|z)\, P(z|\mathrm{DM_{EG}}) dz\, dm_r.$$

This is calculated for each FRB individually, where we use each of the three models for $P(m_r|z)$ described in Section 3.

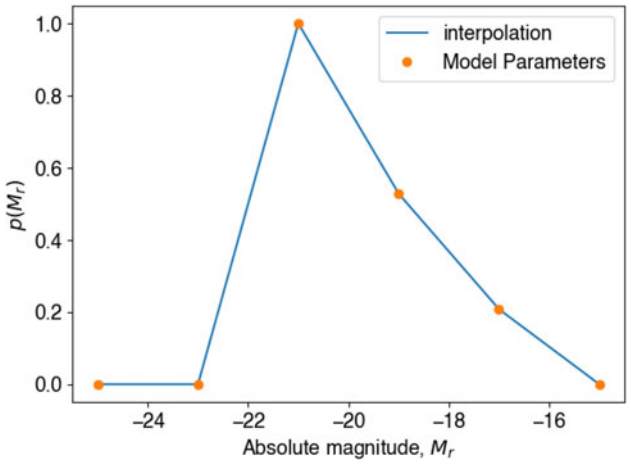


Figure 5. Fitted distribution of best-fit absolute magnitudes M_r for the Naive model developed in this work, showing the model parameters, and the interpolation between them.

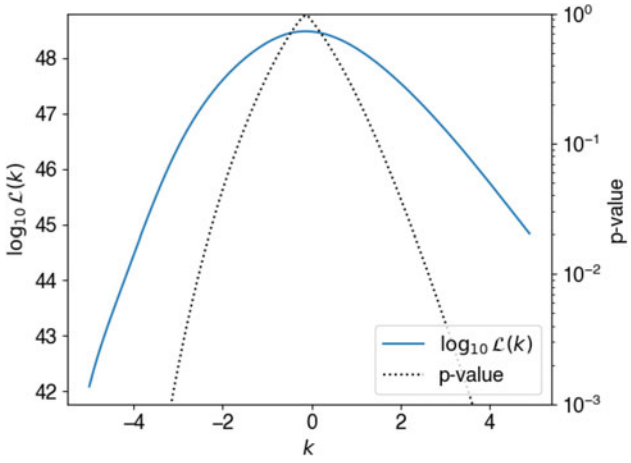


Figure 6. Fitted log likelihood of the Naive model (this work) as a function of k, $\log_{10}\mathcal{L}(k)$, while holding other model parameters fixed at their values given in Figure 5.

5. Results

Our model fitting procedure aims at maximising the likelihood of an observation, $P(\mathbf{x}, N_O)$, given by Equation (10). We evaluate the likelihood on a sample of 32 FRBs with optical data detected during CRAFT ICS observations (Shannon et al. 2025), and maximising with respect to the six values which parameterise the $P(M_r)$ curve in the case of the Naive model, and or f_{sfr} in the case of the Loudas25 model.

In the case of the Naive model, we find that our numerical procedure produces a peak in $P(M_r)$ near $M_r = -21$. Our preliminary investigation (see Appendix 1) found no probability of there being an excess population of very dim ($M_r \geq -15$) or very bright ($M_r < -25$) hosts. However, we find a significant tail towards high magnitude (low-luminosity) hosts. Our best-fit K_r-correction parameter is $k = -0.1$; fixing other model parameters, and varying k, produces the $\mathcal{L}(k)$ curve given in Figure 6. Using Wilks' theorem, $-2\log\mathcal{L}(k_{\mathrm{best}})/\mathcal{L}(k_{\mathrm{true}}) \sim \chi^2_1$, where k_{true} is the true value of k and k_{best} is the best-fit value, for large sample sizes; this allows us to construct a 68% confidence interval for k of $(-1.4, 1.3)$, that is, we find no evidence for a K_r-correction to the FRB absolute host

https://doi.org/10.1017/pasa.2026.10224 Published online by Cambridge University Press

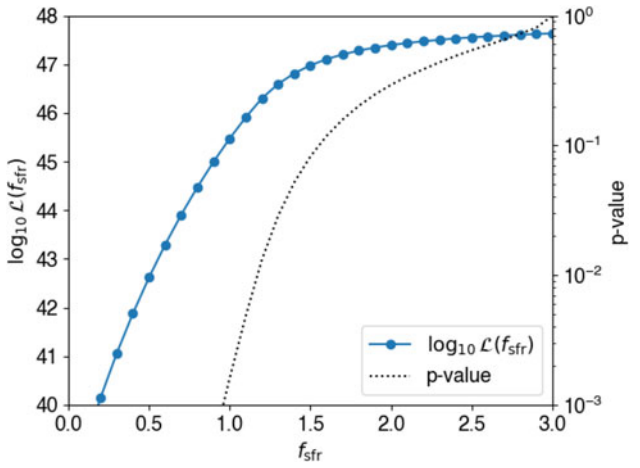


Figure 7. Fitted log likelihood of the Loudas25 model as a function of $f_{\rm sfr}$, $\log_{10}\mathcal{L}(f_{\rm sfr})$.

magnitude distribution. This is not surprising, given that our most likely hosts span only a small redshift range: $z \leq 0.55$ for all but one FRB, and most fall in the range $0.2 \leq z \leq 0.4$.

In the case of the Loudas25 model, we show $\mathcal{L}(f_{\rm sfr})$ in Figure 7. We obtain a best-fit value of $f_{\rm sfr} = 3.0$, the highest value we investigate. Using Wilks' theorem as above, we find a 68% lower bound on $f_{\rm sfr}$ to be 1.7; we exclude that $f_{\rm sfr} \leq 1$ with a p-value of 0.12%, that is, at $3.0\,\sigma$ on a two-sided test. This observation is at odds with the scenario where a fraction of FRBs are stellar-mass tracers, as proposed by Horowicz & Margalit (2026).

We compare the goodness of fit between models both by comparing the peak fitted likelihoods and by comparing the cumulative distributions (CDFs) of our priors and posteriors on $P(m_r)$, summed over all FRB host images. The cumulative distributions $C(m_r)$ predicted by the models are calculated as

$$C(m_r) = N_{\rm FRB}^{-1} \sum_{i=1}^{N_{\rm FRB}} \int_{-\infty}^{m_r} P(O|m_r') P_i(m_r') dm_r', \tag{28}$$

such that

$$C(m_r \to \infty) = N_{\rm FRB}^{-1} \sum_{i=1}^{N_{\rm FRB}} (1 - P_i(U)), \tag{29}$$

where P_i indicates the probability for the ith FRB. The cumulative observed distributions are generated from observed galaxy magnitudes m_r weighted by posterior host probabilities $P(O|\mathbf{x})$. Measuring the maximum differences between the CDFs produces a KS-like statistic (Kolmogorov 1933; Smirnov 1948). However, important exceptions prevent a quantitative interpretation: in these diagrams, both prior and posterior distributions vary with the model; each increment is not of equal value, but weighted by $P(O_i|\mathbf{x}, N_O)$; and the normalisation of each scale is not unity, but is less, due to the probability of the true host being unseen. Nonetheless, smaller values of our KS-like statistic indicate a better fit. We show these values in Figure 8 for all three models, and in Table 3 give the values for the KS-like statistic, and maximum likelihood calculated above. The observed posterior (cumulative) distributions are almost identical, as discussed below in Section 5.1, and visually overlap each other.

Comparing both the KS-like test statistics and log-likelihood values, the Naive model gives a marginally better description of the

Table 3. Value of the KS-like test statistic, and log-likelihood, for the three models considered in this work.

Model	KS	$\log_{10}\mathcal{L}$
Marnoch23	0.078	48.35
Loudas25 ($f_{\rm sfr} = 3.0$)	0.122	47.63
Naive (best fit)	0.079	48.48

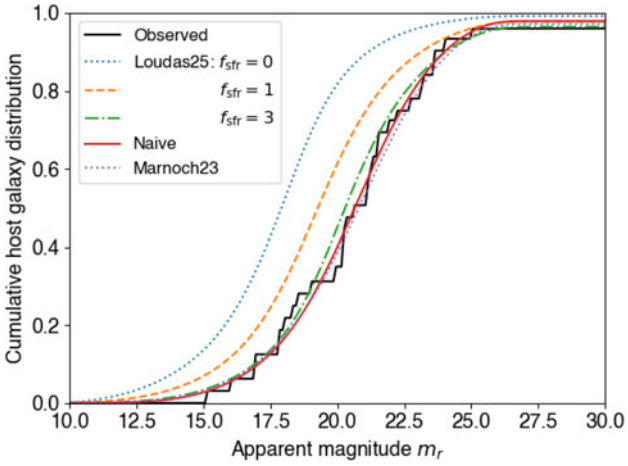


Figure 8. Cumulative observed (posterior) and prior distributions in $P(m_r)$ for ASKAP/CRAFT ICS FRBs according to the Loudas25 model, with $f_{\rm sfr} = 0$ (mass-weighted), $f_{\rm sfr} = 1$ (SFR-weighted), and $f_{\rm sfr} = 3.0$ (best fit); the Naive model developed in this work; and the Marnoch23 model. See text for explanation of calculation.

data than the Marnoch23 model, with the Loudas25 model giving a less good fit. We should bear in mind that the Marnoch23, Loudas25, and Naive models have no, one, and seven degrees of freedom, respectively, although the Marnoch23 model is explicitly fit to photometric data on many FRBs contained in the current sample, and so is not independent. We currently do not have a statistic by which we can compare likelihoods between models, so cannot assess whether or not the relative likelihoods, given the number of degrees of freedom, is evidence for or against any given model. Nonetheless, given that the Marnoch23 model has both fewer degrees of freedom and gives at least an equally good fit as other models, we suggest that this should be considered the default model.

We present the $P(m_r|z)$ distributions for the three models in Figure 9, using the best-fitting for the Naive and Loudas25 models, and also that for the Loudas25 model with $f_{\rm sfr} = 1$, at characteristic values of $z = 0.1$ and $z = 1.0$. Notably, the Loudas25 $f_{\rm sfr} = 1$ model predicts FRB hosts to have much smaller magnitudes (i.e. be much brighter) than any of the models fit to data. By weighting the galaxy population selected by SFR($f_{\rm sfr} = 1$), the Loudas25 model predicts brighter galaxies than unweighted galaxy populations. Clearly, the seemingly unphysical best-fit value of $f_{\rm sfr=3}$ is the Loudas25 model attempting to construct a $P(m_r)$ distribution with fainter galaxies than that predicted by SFR alone, while suppressing the abundance of brighter ones (which are likely associated with high-SFR, high-mass galaxies).

The difference between an SFR-weighted population and the best-fit models increases with redshift: at $z = 0.1$, the three fitted distributions are very similar, whereas by $z = 1.0$, the Loudas25, Naive, and Marnoch23 models produce increasingly faint distributions. Since only one FRB in our data sample (FRB 20220610A,

https://doi.org/10.1017/pasa.2026.10224 Published online by Cambridge University Press

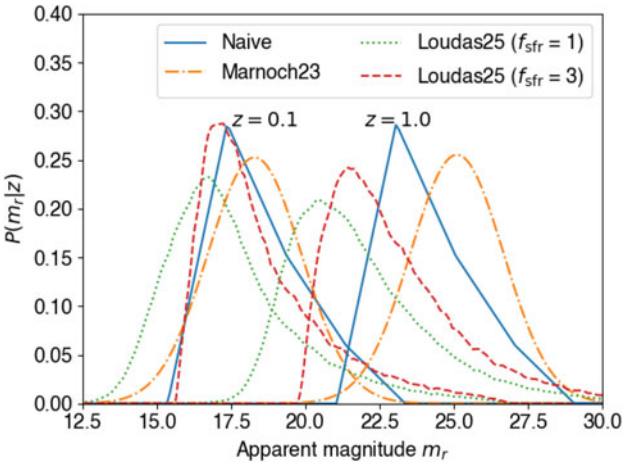


Figure 9. Apparent magnitude distributions, $P(m_r|z)$, produced by the empirical Marnoch23 model based on data from Marnoch et al. (2023); the predictive Loudas25 models based on star-formation rate ($f_{sfr} = 1$), and the best-fit value ($f_{sfr} = 3$) from Loudas et al. (2025); and a Naive model developed in this work (see text).

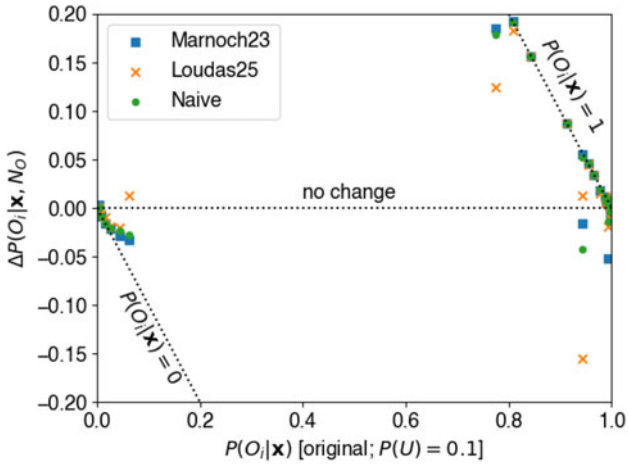


Figure 10. Change in posterior confidence $\Delta P(O_i|\mathbf{x}, N_O)$ as a function of posterior values $P(O_i|\mathbf{x}, N_O)$ calculated from the original PATH methodology, as per the Marnoch23, Loudas25, and Naive models with best-fit values. Positive values indicate increased confidence.

at $z = 1.016$ Ryder et al. 2023; Gordon et al. 2024) contains a probable host galaxy with measured magnitude at $z > 0.53$, and the model predictions diverge at high redshift, we urge caution in interpreting our results in the $z \gtrsim 0.5$ range.

5.1. Updating FRB host galaxy predictions

So far in this work, we have phrased our conclusions in terms of 'what is the intrinsic magnitude distribution of FRB host galaxies?'. However, for those groups using PATH to identify the most likely FRB hosts, a much more relevant conclusion is: 'how does this change our conclusions on true FRB hosts'?

In Figure 10, we give the distribution of posterior $P(O_i|\mathbf{x})$ values for ICS FRBs using a standard PATH analysis. Like Shannon et al. (2025), we use an offset prior with a scale factor of half of the galaxy's half-light radius. Unlike Shannon et al. (2025), we use $P(U) = 0.1$, due to the dangers of using $P(U) = 0$ noted by B. C. Andersen et al. (in preparation). We show the change in posterior values, $\Delta P(O_i|\mathbf{x}, N_O)$, when using the Marnoch23 and best-fit Naive and Loudas25 $f_{sfr} = 3.0$ models. To guide the eye, we plot loci corresponding to the cases where the new posterior estimates $P(O_i|\mathbf{x})$ are zero and unity. Reassuringly, all models give broadly similar results, identifying the same most probable hosts as those previously produced by PATH: we give updated values in Table A1. Furthermore, all three models produce near-identical posteriors which tend to increase our posterior likelihoods, with many previously likely host candidates being promoted to the $P(O_i|\mathbf{x}) = 1$ line, and many previously unlikely candidates being demoted to the $P(O_i|\mathbf{x}) = 0$ line. In particular, FRBs 20210807D and 20240210A, which under a PATH analysis with $P(U) = 0.1$ do not meet the usual criteria of $P(O|x) \geq 0.95$ for 'firm' host galaxy associations (with most probable hosts having $P(O|x) = 0.843$ and 0.718, respectively), have $P(O|x) = 1.00$ for all three models used here, validating the choice of $P(U) = 0$ by Shannon et al. (2025). FRB 20181112A previously had $P(O|x) = 0.775$, with the Loudas25 model producing $P(O|x) = 0.896$, and the Marnoch23 and Naive models producing $P(O|x) = 0.960$ and 0.953, respectively; given that the latter give better fits, we suggest this also be considered a firm host identification. Our updated model also confirms the result from Marnoch et al. (2023) that there are no viable candidates for FRB 20210912A, with all models agreeing on $P(U|x) = 1$. Finally, we confirm the host galaxy of FRB 20190611B ($P(O|x) \geq 0.957$), the identification of which had been called into question by Cordes et al. (2022) due to its relatively high redshift for its DM, and significant scattering value.

5.2. Well-justified unseen priors

Previous uses of PATH have chosen a variety of values for the unseen prior, $P(U)$, ranging from 0 (e.g. Shannon et al. 2025) to $P(U) = 0.2$ by Sharma et al. (2024); only Caleb et al. (2025), who also used the results of Marnoch et al. (2023), have estimated $P(U)$ based on an assumed host galaxy distribution and FRB redshift.

Here, we can readily test these assumptions. In Figure 11 we plot $P(U|\mathrm{DM_{EG}})$ as a function of $\mathrm{DM_{EG}}$ for all three fit models (giving $P(m_r|\mathrm{DM_{EG}})$) and optical depths (giving $P(O|m_r)$) used here, for the ASKAP/ICS observations at ~ 900 MHz, CHIME observations at $\delta = 60°$, MeerKAT coherent detections, and DSA-110.

For some critical value of $\mathrm{DM_{EG}}$, the function $P(z|\mathrm{DM_{EG}})$ calculated by zDM will predict a decreasing z with increasing $\mathrm{DM_{EG}}$. This is due to the probability of detecting a necessarily very bright FRB from a very large distance becoming less than the probability of a large over-fluctuation in DM from a nearby FRB. While the exact behaviour of this effect depends on the FRB luminosity function, frequency dependence, DM host contribution, and FRB population evolution (James et al. 2022), it will occur at lower values of $\mathrm{DM_{EG}}$ for less-sensitive instruments. The consequence is that FRBs with very high $\mathrm{DM_{EG}}$ are predicted to have lower redshift and therefore brighter apparent magnitudes, that is, they will be easier to detect despite their very high DM values. Using the FRB population parameter fits of Hoffmann et al. (2026), this effect becomes significant in the ASKAP ICS survey for $\mathrm{DM_{EG}} > 1\,000$ pc cm^{-3}, and $> 1\,500$ pc cm^{-3} for CHIME, but is not relevant for $\mathrm{DM_{EG}} < 2\,000$ pc cm^{-3} for MeerKAT or DSA-100. Different models for the $P(m_r|z)$ distribution also produce significantly different predictions for $\mathrm{DM_{EG}} \gtrsim 500$. Combined with the aforementioned uncertainties in the $P(z|\mathrm{DM_{EG}})$, we again highlight that the predictions from this work should be treated with caution in this regime.

https://doi.org/10.1017/pasa.2026.10224 Published online by Cambridge University Press

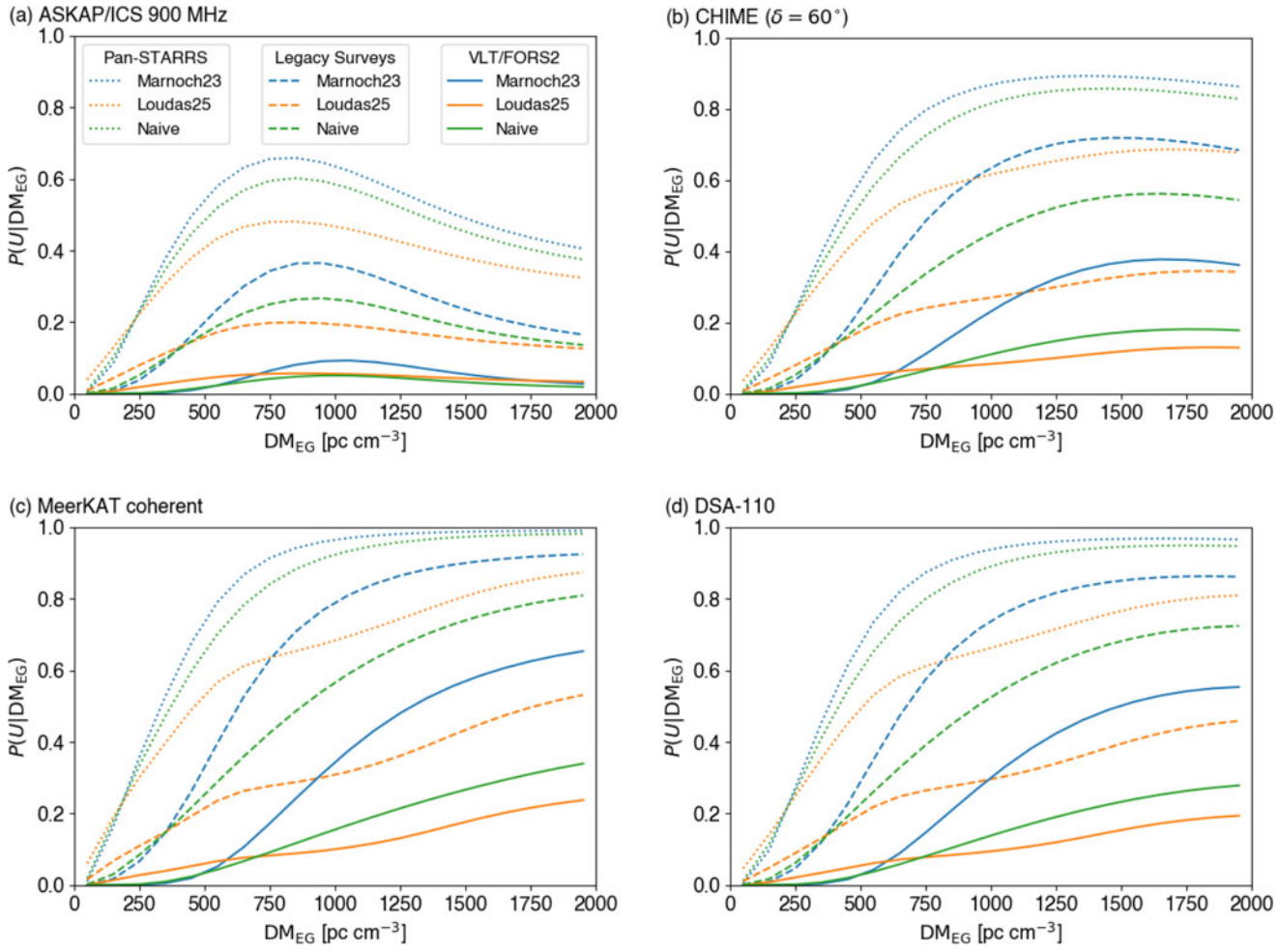


Figure 11. Estimated probabilities, $P(U|DM_{EG})$, of the true host being unseen in an optical image as a function of extragalactic DM, DM_{EG}, for each of the three host models developed in this work, and three optical follow-up sensitivities, shown for: (a) ASKAP ICS observations at 892 MHz; (b) CHIME observations at a declination of $\delta = 60°$; (c) MeerKAT coherent detection; and (d) DSA-110.

With these caveats, we observe that $P(U)$ is highly DM-dependent, such that setting $P(U)$ constant for an FRB survey with a large range of FRB DMs (as is usually performed in the literature) is ill-advised. In the case of surveys such as Pan-STARRS, $P(U)$ will reach 50% by a relatively modest $DM_{EG} = 500$ pc cm^{-3}, while observations with VLT/FORS2 produce $P(U) \lesssim 0.05$ in this range. Thus we recommend re-running PATH on FRB samples from existing surveys, for example, the DSA FRB samples of Sharma et al. (2024) and Connor et al. (2025), or the MeerKAT FRBs of Jankowski et al. (2023) and Pastor-Marazuela et al. (2026), to generate more-robust host associations. Due to its simplicity, we recommend using the Marnoch23 model to generate PATH priors. However, a more thorough approach would use all three models, and treat the variation in host galaxy posteriors between them as a model systematic. This methodology should also be relevant to localisations with CHIME outriggers (CHIME/FRB Collaboration et al. 2025), and perhaps very low-DM CHIME FRBs detected without baseband data (e.g. Bhardwaj et al. 2024).

5.3. Accounting for redshift

Our updates to PATH assume that an optical image is being analysed with no redshift information available. This is because PATH was designed to identify a most likely host for further spectroscopic follow-up, meaning that no spectroscopic information should be assumed when running it. Furthermore, when performing FRB follow-up, spectroscopic data is usually obtained only for the most probable host galaxy for that FRB.

In a future work, we aim to develop methods to incorporate partial redshift information into our likelihood estimates. For now, we show the predicted $P(m_r|z)$ distributions of FRB hosts for each of our models in Figure 12, and compare these to measured redshifts of FRB hosts from major surveys. While it appears that the high-redshift FRB hosts identified by MeerTRAP and DSA are brighter than those predicted by the Marnoch23 and Naive models, and agree better with the Loudas25 model, we note that both samples are incomplete, with only those FRBs with detectable hosts being published (the majority of these measurements were taken with an r-band filter, so we discount this as a source of discrepancies). A counter-example is FRB 20240304B with $DM_{EG} = 2\,390$ pc cm^{-3}, where Caleb et al. (2025) report a relatively faint most probable host at $z = 2.148$, having $m_{F200W} = 27.82$ and $m_{322W2} = 28.72$. This emphasises another source of bias not yet discussed in this work (reporting bias), and hence the importance of publishing all FRB detections, and optical follow-up data, irrespective of whether or not a probable host has been identified.

https://doi.org/10.1017/pasa.2026.10224 Published online by Cambridge University Press

6. Discussion and conclusion

We have extended the PATH framework to allow for models of expected galaxy properties to be incorporated into FRB host identification in optical images. This framework allows for a robust, and physically consistent, method of determining priors that an FRB host galaxy is unseen in optical images with arbitrary magnitude limits, thereby allowing data from an increased range of experiments to be used in both FRB host galaxy and population studies, and systematics due to unseen hosts to be explicitly accounted for.

We have considered three models for the true distribution of FRB host galaxy *r*-band magnitudes: the 'Marnoch23' model of James et al. (2026) based on Marnoch et al. (2023), which is an empirical fit to known FRB hosts; the 'Loudas25' model based on Loudas et al. (2025), which weights the galaxy population by a linear combination of stellar mass and SFR; and the 'Naive' model based on absolute galaxy magnitudes, developed in this work. The parameters of the latter two are fit to the observed host galaxy properties of 32 FRBs detected by ASKAP/ICS observations.

Incorporating these models into PATH, we recalculated the probabilities of candidate galaxies being the true host for FRBs detected by the ASKAP/CRAFT ICS system. We find that all three models tend to increase the confidence in previously-identified most likely hosts. Using the Loudas25 model, we find strong evidence (p-value 0.86%) that the true distribution of FRB host galaxies is fainter than that predicted by star-formation, and overwhelming evidence (p-value 10^{-9}) that it is fainter than that of a stellar-mass weighting. Using the Marnoch23 and Naive models, both of which give more likely fits, predict an even fainter distribution of FRB hosts, especially at higher redshifts. Due to its simplicity, we recommend using the Marnoch23 model to generate FRB host galaxy priors within the PATH framework, although using the Loudas25 and Naive models will help to evaluate model systematics.

We consider two broad explanations regarding the relative faintness of the FRB host distribution. Firstly, this effect may be due to, for example, a metallicity preference in FRB hosts, as suggested by Sharma et al. (2024). However, here we invoke it due to an *excess* of dim FRB hosts, rather than a deficit. It is in principle possible to extend the Loudas25 model to a 2D distribution in (SFR, M*) space, which would then include metallicity either implicitly or explicitly. We might also weight by star-formation history, for example, via an exponential time-delay representing merger scenarios, by building in a model of each galaxy's evolution.

Secondly, another possible explanation is that the apparent excess of dim hosts is in fact a deficit of bright ones caused by FRB selection effects. FRB detection experiments are known to be biased against highly scattered FRBs, since scattering smears the burst fluence (i.e. the signal) over a longer time-duration (i.e. more noise) (Cordes & McLaughlin 2003). Larger host galaxies would be expected to result in more-scattered FRBs, potentially due to having more turbulent, ionised gas, but also due to a larger geometric lever-arm between the FRB location and the host interstellar medium. This would then reduce the rate of FRBs detected from these galaxies, similarly to the rate reduction viewed by CHIME through the plane of the Milky Way (CHIME/FRB Collaboration et al. 2026) and the Cygnus region (Patil et al. 2026). A correlation between galaxy inclination and scattering has been reported by Bhardwaj et al. (2024), which is consistent with such a scattering-bias effect, although there is no direct evidence for a correlation between FRB scattering properties and other FRB host properties such as stellar mass (Glowacki et al. 2025).

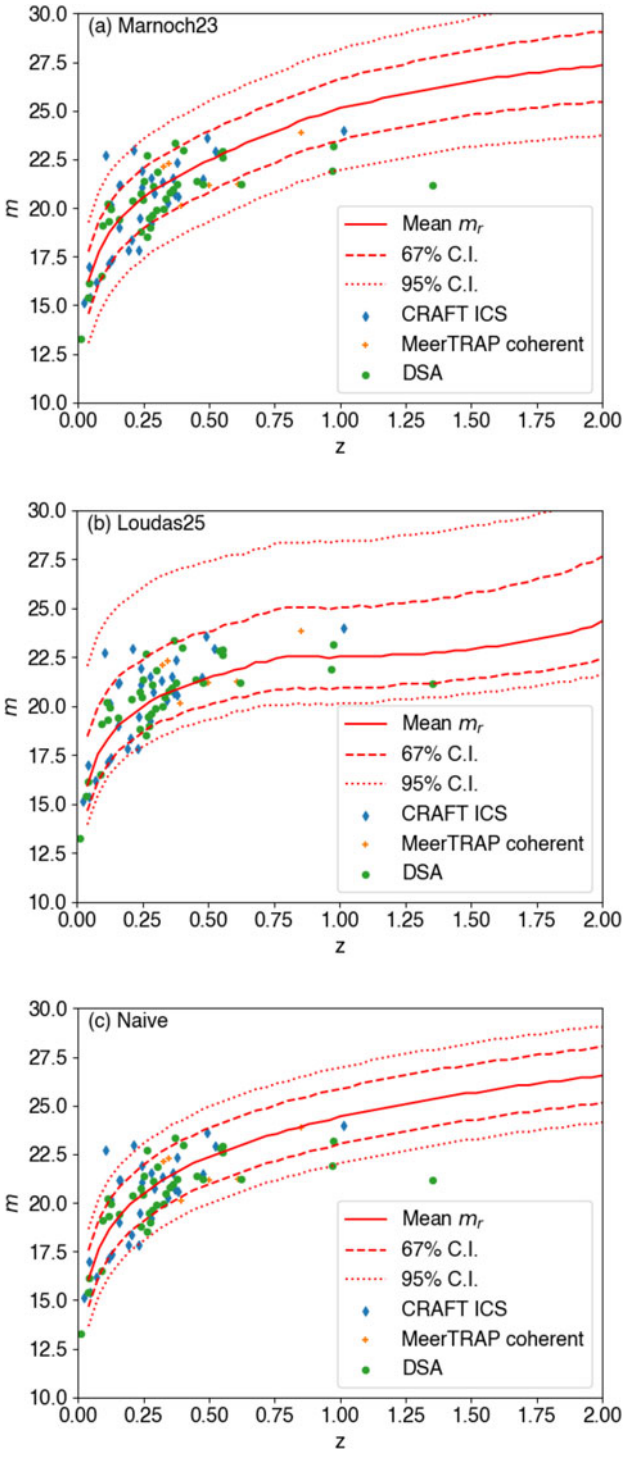


Figure 12. Mean, and 67% ($\pm1\sigma$) and 95% confidence ($\pm2\sigma$) intervals, of the FRB *r*-band host galaxy magnitude distribution, m_r, as a function of redshift, using Marnoch23, Loudas25, and Naive models. Also shown are observed magnitudes for probable FRB host galaxies (measured using a variety of filters) for FRBs detected in CRAFT ICS (Shannon et al. 2025), MeerTRAP coherent (Pastor-Marazuela et al. 2026), and DSA (Sharma et al. 2024; Connor et al. 2025) observations.

Given that most of the data used to construct our models were from the relatively nearby Universe ($z \lesssim 0.5$), our host models begin to diverge at high redshifts, and we do not consider our

https://doi.org/10.1017/pasa.2026.10224 Published online by Cambridge University Press

predictions reliable for $z \geq 1$. Of great benefit would be incorporating fits to data from DSA-110 and MeerTRAP, which probe to higher redshifts than ASKAP, and would allow sufficient data to properly fit for the extended parameter space. We have also made several approximations when scaling observed galaxy magnitudes in other bands to r-band magnitudes, in which our models are specified. A more complete model would directly estimate magnitudes in multiple filters. Another extension of this work would be to enable the zDM code, which we use to predict the redshift distributions of FRB hosts, to accept host galaxy candidate posterior probabilities, and calculate updated redshift distributions for FRBs with unseen host galaxies. This would allow the incorporation of data where the true FRB host is too faint to detect in optical observations, or where the identification of the true host is uncertain. Doing so would both allow and require the FRB host galaxy distribution, and FRB population, to be simultaneously fit, which is a complex task that we leave to a future work.

For now, we encourage the updated version of PATH to be used for FRB host galaxy identification, and have made available code allowing the use of each model.

Acknowledgements. We would like to thank the anonymous referee for their constructive feedback that helped us improve the clarity of this work. NL acknowledges support from the Venture Forward Fellowship of the Department of Astrophysical Sciences at Princeton University.

Data availability statement. The data and results from this work can be obtained from the zDM GitHub codebase (James et al. 2021), at https://github.com/FRBs/zdm.

Funding statement. The authors declare no external sources of funding.

Competing interests. The authors declare no competing interests.

References

Aggarwal, K., Budavári, T., Deller, A. T., Eftekhari, T., James, C. W., Prochaska, J. X., & Tendulkar, S. P. 2021, ApJ, 911, 95
Appenzeller, I., & Rupprecht, G. 1992, Msngr, 67, 18
Bertin, E., Schefer, M., Apostolakos, N., Álvarez-Ayllón, A., Dubath, P., & Kümmel, M. 2020, in Astronomical Data Analysis Software and Systems XXIX, Vol. 527, Astronomical Society of the Pacific Conference Series, ed. R. Pizzo, E. R. Deul, J. D. Mol, J. de Plaa, & H. Verkouter, 461
Bhandari, S., et al. 2022, AJ, 163, 69
Bhandari, S., et al. 2020, ApJ, 895, L37
Bhardwaj, M., Lee, J., & Ji, K. 2024, Natur, 634, 1065
Bhardwaj, M., et al. 2024, ApJ, 971, L51
Blanton, M. R., et al. 2003, ApJ, 594, 186
Bochenek, C. D., Ravi, V., Belov, K. V., Hallinan, G., Kocz, J., Kulkarni, S. R., & McKenna, D. L. 2020, Natur, 587, 59
Caleb, M., et al. 2025, https://doi.org/10.48550/arXiv.2508.01648
Chambers, K. C., et al. 2016, https://doi.org/10.48550/arXiv.1612.05560
Chatterjee, S., et al. 2017, Natur, 541, 58
CHIME/FRB Collaboration, et al. 2026, https://doi.org/10.48550/arXiv.2601.09399
CHIME/FRB Collaboration, et al. 2025, ApJS, 280, 6
CHIME/FRB Collaboration, et al. 2020, Natur, 587, 54
Connor, L. 2019, MNRAS, 487, 5753
Connor, L., et al. 2025, NatAs, 9, 1226
Cordes, J. M., & Lazio, T. J. W. 2003, https://doi.org/10.48550/arXiv.astro-ph/0301598
Cordes, J. M., & McLaughlin, M. A. 2003, ApJ, 596, 1142
Cordes, J. M., Ocker, S. K., & Chatterjee, S. 2022, ApJ, 931, 88
Dey, A., et al. 2019, AJ, 157, 168
Driver, S. P., et al. 2016, ApJ, 827, 108
Farah, W., et al. 2018, MNRAS, 478, 1209
Gardenier, D. W., van Leeuwen, J., Connor, L., & Petroff, E. 2019, A&A, 632, A125
Glowacki, M., et al. 2024, ApJ, 962, L13
Glowacki, M., et al. 2025, PASA, 42, e157
Gordon, A. C., et al. 2023, ApJ, 954, 80
Gordon, A. C., et al. 2024, ApJ, 963, L34
Heintz, K. E., et al. 2020, ApJ, 903, 152
Hoffmann, J. L., James, C., Glowacki, M., Prochaska, X., Gordon, A., Deller, A., Shannon, R. M., & Ryder, S. 2025, PASA, 42, e017
Hoffmann, J. L., James, C., Prochaska, X., & Glowacki, M. 2026, PASA, 43, e017
Horowicz, A., & Margalit, B. 2026, ApJ, 996, 78
James, C. W., et al. 2022, MNRAS, 516, 4862
James, C. W., Prochaska, J. X., & Ghosh, E. M. 2021, https://zenodo.org/record/5213780#.YRxh5BMzZKA. V.0.1, August 18, 2021.
James, C. W., Prochaska, J. X., Macquart, J.-P., North-Hickey, F. O., Bannister, K. W., & Dunning, A. 2022, MNRAS, 509, 4775
James, C. W., et al. 2026, arXiv e-prints (February): arXiv:2603.00371.
Jankowski, F., et al. 2023, MNRAS, 524, 4275
Kim, J., et al. 2023, ApJ, 951, 137
Kirsten, F., et al. 2022, Natur, 602, 585
Kolmogorov, A. 1933, GIIA, 4, 83
Kümmel, M., Bertin, E., Schefer, M., Apostolakos, N., Álvarez-Ayllón, A., & Dubath, P. 2020, in Astronomical Data Analysis Software and Systems XXIX, Vol. 527, Astronomical Society of the Pacific Conference Series, ed. R. Pizzo, E. R. Deul, J. D. Mol, J. de Plaa, & H. Verkouter, 29
Laigle, C., et al. 2016, ApJS, 224, 24
Leja, J., Johnson, B. D., Conroy, C., van Dokkum, P. G., & Byler, N. 2017, ApJ, 837, 170
Leja, J., et al. 2022, ApJ, 936, 165
Lorimer, D. R., Bailes, M., McLaughlin, M. A., Narkevic, D. J., & Crawford, F. 2007, Sci, 318, 777
Loudas, N., Li, D., Strauss, M. A., & Leja, J. 2025, ApJ, 991, 85
Luo, R., Men, Y., Lee, K.,Wang, W., Lorimer, D. R., & Zhang, B. 2020, MNRAS, 494, 665
Macquart, J.-P., et al. 2020, Natur, 581, 391
Marnoch, L., et al. 2023, MNRAS, 525, 994
Michilli, D., et al. 2018, Natur, 553, 182
Moroianu, A. M., et al. 2026, ApJ, 996, L16
Niu, C.-H., et al. 2022, Natur, 606, 873
Niu, C.-H., et al. 2026, SciB, 71, 76
Ocker, S. K., & Cordes, J. M. 2026, ApJ, 1002, 3
Pastor-Marazuela, I., et al. 2026, MNRAS, 545, staf2144
Patil, S. S., et al. 2026, ApJ, 997, L5
Planck Collaboration, et al. 2016, A&A, 594, A13
Ryder, S. D., et al. 2023, Sci, 382, 294
Shannon, R. M., et al. 2018, Natur, 562, 386
Shannon, R. M., et al. 2025, PASA, 42, e036
Sharma, K., et al. 2026, https://doi.org/10.48550/arXiv.2605.01994
Sharma, K., et al. 2024, Natur, 635, 61
Shin, K., et al. 2023, ApJ, 944, 105
Skelton, R. E., et al. 2014, ApJS, 214, 24
Smirnov, N. 1948, AMS, 19, 279
Yamasaki, S., Hashimoto, T., Kusakabe, H., & Goto, T. 2026, ApJ, 997, L6

Appendix 1. Binning in the Naive model

Our Naive model, described in Section 3.3, is parameterised by an arbitrary number of bins, $N_{\rm bins}$, in absolute magnitude space. There is no a priori prescription for the 'correct' number of bins, or the correct minimum and maximum absolute magnitudes to use. Good statistical practice suggests that the total number of bins remains significantly smaller than the number of FRBs we analyse

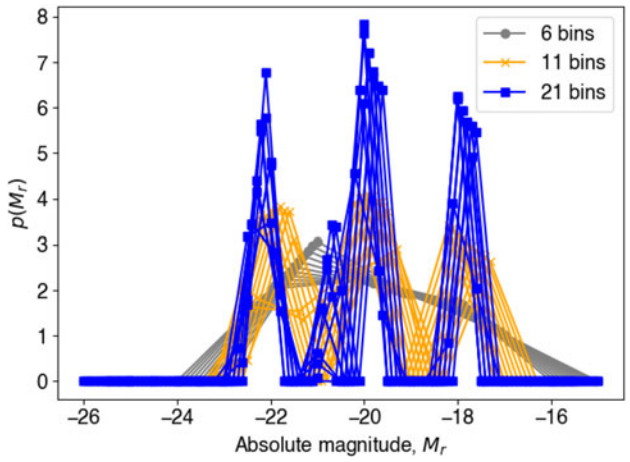


Figure A1. Best fitting distributions $P(M_r)$ found for various combinations of $N_{\rm bins}$, $M_r^{\rm min}$, and $M_r^{\rm max}$.

here (32), while we wish to retain sufficiently many to allow the model to be flexible enough to describe the (unknown) FRB host galaxy distribution. Here we test the effects of this arbitrariness, to determine how robust our conclusions are against variations in these parameters.

We first tried $N_{\rm bins} = 10$, the range $M_r^{\rm max} = -30$, $M_r^{\rm min} = -10$, and the fitting procedure of Section 4, and found that the model never predicts any probability of $M_r < -25$ or $M_r > -15$. We then investigated the effects of bin location and number by varying $M_r^{\rm min}$ from -26 to -25 in increments of 0.1, setting $M_r^{\rm max} = M_r^{\rm min} + 10$, and consider $N_{\rm bins} = \{6, 11, 21\}$ (i.e. bin spacings of 2, 1, and 0.5 magnitudes). Running these 33 scenarios produced the set of best-fit M_r distributions shown in Figure A1. We find that as $N_{\rm bins}$ increases, the model predicts more spiky structures in $P(M_r)$, which we interpret as the model over-fitting the data. We find the best-fit log-likelihood to increase with $N_{\rm bins}$, as expected for greater degrees of freedom, and to vary with exact placement by ± 0.1.

We can use Wilks' theorem to determine the significance of increasing the number of bins, since halving the bin spacing preserves the locations of the original bins in magnitude space, that is, it produces a nested model. Doing so shows that the increased likelihood with increasing bins is negligible, and would occur at least 96% of the time under the null hypothesis that the 6-bin model correctly describes the data. While Wilks' theorem is only valid as the number of data points tends to infinity, our complete lack of evidence for a significant increase in explanatory power with increased model bins makes us confident in our conclusion. We therefore use six bins for our analysis. We consider that fewer than six bins results in insufficient flexibility, which is the purpose of this model.

Table A1. Updated FRB PATH associations, giving priors and posteriors for the traditional PATH analysis with $P(U) = 0.1$, and our three models for $p(m)$, using best-fit values for the Loudas and naive models (see text). Only galaxies with $P(O|\mathbf{x}) > 10^{-4}$ in at least one model are reported. Note that $P(O)$ values in the original PATH analysis include the Σ_j values, but have been renormalised according to Equation (2), while other $P(O)$ values do not include the equivalent factor, $\rho(m)$.

TNS name					Original PATH		Marnoch23		Loudas25		Naive	
RA_{cand}	Dec_{cand}	θ	ϕ	mag	$P(U)$	$P(U\|\mathbf{x})$	$P(U)$	$P(U\|\mathbf{x})$	$P(U)$	$P(U\|\mathbf{x})$	$P(U)$	$P(U\|\mathbf{x})$
(deg)	(deg)	(")	(")		$P(O)$	$P(O\|\mathbf{x})$	$P(O)$	$P(O\|\mathbf{x})$	$P(O)$	$P(O\|\mathbf{x})$	$P(O)$	$P(O\|\mathbf{x})$
FRB20180924B					0.100	0.002	0.001	0.000	0.024	0.000	0.003	0.000
326.1052	−40.9002	0.79	1.00	19.98	0.870	0.998	0.197	1.000	0.163	1.000	0.191	1.000
FRB20181112A					0.100	0.138	0.026	0.007	0.054	0.019	0.029	0.008
327.3486	−52.9709	0.40	0.68	21.58	0.078	0.775	0.195	0.960	0.145	0.900	0.200	0.953
327.3496	−52.9696	5.36	1.06	19.22	0.757	0.061	0.085	0.029	0.175	0.074	0.103	0.034
327.3467	−52.9704	4.24	0.28	25.67	0.003	0.026	0.008	0.004	0.009	0.007	0.009	0.005
327.3483	−52.9729	7.03	0.62	22.06	0.051	0.000	0.198	0.000	0.119	0.000	0.172	0.000
FRB20190102C					0.100	0.003	0.001	0.000	0.022	0.002	0.003	0.000
322.4153	−79.4758	0.34	0.87	21.25	0.744	0.997	0.145	1.000	0.087	0.998	0.115	1.000
FRB20190608B					0.100	0.034	0.001	0.000	0.022	0.000	0.003	0.000
334.0204	−7.8988	2.87	1.66	17.15	0.893	0.966	0.092	1.000	0.107	1.000	0.096	1.000
FRB20190611B					0.100	0.031	0.000	0.001	0.016	0.035	0.002	0.003
320.7428	−79.3973	2.15	0.56	23.09	0.334	0.943	0.041	0.999	0.041	0.956	0.049	0.996
320.7440	−79.3984	3.28	0.31	25.60	0.048	0.016	0.001	0.000	0.012	0.007	0.002	0.001
320.7497	−79.3972	3.13	0.28	26.76	0.022	0.008	0.000	0.000	0.001	0.002	0.000	0.000
320.7383	−79.3976	4.85	0.39	24.28	0.127	0.000	0.009	0.000	0.025	0.000	0.019	0.000
FRB20190711A					0.100	0.014	0.023	0.059	0.053	0.189	0.027	0.080
329.4195	−80.3581	1.43	0.58	24.37	0.409	0.942	0.073	0.927	0.043	0.788	0.060	0.900
329.4121	−80.3571	4.58	0.56	25.45	0.190	0.043	0.013	0.015	0.015	0.023	0.015	0.020
FRB20190714A					0.100	0.003	0.011	0.000	0.043	0.000	0.016	0.000
183.9795	−13.0211	0.81	0.93	19.56	0.707	0.997	0.135	1.000	0.225	1.000	0.174	1.000

https://doi.org/10.1017/pasa.2026.10224 Published online by Cambridge University Press

Table A1. Continued.

TNS name					Original PATH		Marnoch23		Loudas25		Naive	
RA_{cand}	Dec_{cand}	θ	ϕ	mag	$P(U)$	$P(U\|\mathbf{x})$	$P(U)$	$P(U\|\mathbf{x})$	$P(U)$	$P(U\|\mathbf{x})$	$P(U)$	$P(U\|\mathbf{x})$
(deg)	(deg)	(")	(")		$P(O)$	$P(O\|\mathbf{x})$	$P(O)$	$P(O\|\mathbf{x})$	$P(O)$	$P(O\|\mathbf{x})$	$P(O)$	$P(O\|\mathbf{x})$
FRB20191001A					0.100	0.006	0.009	0.000	0.039	0.000	0.013	0.000
323.3519	−54.7485	0.97	1.35	17.81	0.457	0.993	0.065	0.999	0.079	0.999	0.066	0.999
323.3486	−54.7482	6.49	1.45	17.83	0.443	0.001	0.066	0.001	0.080	0.001	0.067	0.001
FRB20191228A					0.100	0.192	0.000	0.000	0.016	0.009	0.002	0.001
344.4308	−29.5943	1.12	0.31	22.53	0.011	0.808	0.037	1.000	0.040	0.991	0.046	0.999
FRB20200430A					0.100	0.003	0.002	0.000	0.027	0.001	0.005	0.000
229.7064	12.3766	1.07	0.69	20.69	0.826	0.997	0.186	1.000	0.126	0.999	0.161	1.000
FRB20200906A					0.100	0.004	0.019	0.000	0.047	0.001	0.022	0.000
53.4958	−14.0832	1.12	1.35	19.63	0.879	0.996	0.122	1.000	0.211	0.999	0.154	1.000
FRB20210117A					0.100	0.004	0.076	0.009	0.071	0.014	0.055	0.008
339.9795	−16.1515	0.91	0.51	22.95	0.512	0.996	0.193	0.991	0.114	0.986	0.158	0.992
FRB20210320C					0.100	0.002	0.002	0.000	0.025	0.000	0.004	0.000
204.4589	−16.1226	0.47	1.02	19.23	0.813	0.998	0.175	1.000	0.212	1.000	0.198	1.000
FRB20210807D					0.100	0.157	0.000	0.000	0.001	0.000	0.001	0.000
299.2201	−0.7623	4.83	2.32	17.35	0.671	0.843	0.160	1.000	0.120	1.000	0.140	1.000
FRB20210912A					0.100	1.000	0.273	1.000	0.096	1.000	0.134	1.000
FRB20211127I					0.100	0.088	0.000	0.000	0.007	0.000	0.001	0.000
199.8082	−18.8379	2.18	5.07	15.38	0.245	0.912	0.100	1.000	0.101	1.000	0.100	1.000
199.8080	−18.8402	8.78	2.28	18.34	0.008	0.000	0.185	0.000	0.159	0.000	0.175	0.000
FRB20211203C					0.100	0.002	0.024	0.000	0.050	0.000	0.026	0.000
204.5626	−31.3801	0.54	0.89	20.25	0.789	0.998	0.112	1.000	0.204	1.000	0.141	1.000
FRB20211212A					0.100	0.009	0.000	0.000	0.005	0.000	0.001	0.000
157.3509	1.3608	1.45	2.72	16.21	0.900	0.991	0.154	1.000	0.171	1.000	0.167	1.000
FRB20220105A					0.100	0.023	0.027	0.004	0.054	0.008	0.029	0.004
208.8038	22.4665	1.83	0.90	21.53	0.512	0.977	0.168	0.996	0.188	0.992	0.213	0.996
FRB20220501C					0.100	0.001	0.005	0.000	0.034	0.000	0.009	0.000
352.3792	−32.4907	0.30	0.90	20.57	0.900	0.999	0.192	1.000	0.158	1.000	0.194	1.000
FRB20220610A					0.100	0.007	0.294	0.059	0.102	0.026	0.145	0.021
351.0735	−33.5137	0.76	1.02	23.96	0.250	0.993	0.133	0.941	0.109	0.974	0.191	0.979
FRB20220725A					0.100	0.003	0.000	0.000	0.015	0.000	0.002	0.000
353.3154	−35.9903	0.50	1.77	17.83	0.898	0.997	0.126	1.000	0.154	1.000	0.139	1.000
FRB20220918A					0.100	0.011	0.045	0.002	0.063	0.005	0.040	0.003
17.5917	−70.8114	0.49	0.45	23.60	0.069	0.989	0.188	0.998	0.104	0.995	0.140	0.997
FRB20221106A					0.100	0.008	0.001	0.000	0.022	0.000	0.003	0.000
56.7045	−25.5696	1.33	2.50	18.34	0.850	0.988	0.117	0.993	0.154	0.996	0.130	0.995
56.7057	−25.5701	3.24	1.07	21.07	0.050	0.004	0.184	0.007	0.124	0.003	0.155	0.005
FRB20230526A					0.100	0.002	0.000	0.000	0.017	0.000	0.002	0.000
22.2326	−52.7175	0.51	0.78	21.15	0.490	0.998	0.157	1.000	0.099	1.000	0.126	1.000
FRB20230708A					0.100	0.008	0.002	0.000	0.027	0.001	0.005	0.000
303.1155	−55.3563	0.14	0.58	22.73	0.079	0.992	0.119	1.000	0.072	0.999	0.096	1.000
FRB20230902A					0.100	0.002	0.004	0.000	0.033	0.001	0.008	0.000
52.1400	−47.3335	0.54	0.68	21.52	0.586	0.998	0.192	1.000	0.136	0.999	0.175	1.000
FRB20231226A					0.100	0.012	0.001	0.000	0.019	0.000	0.002	0.000
155.3639	6.1097	1.99	1.79	19.01	0.845	0.988	0.161	1.000	0.209	1.000	0.185	1.000

https://doi.org/10.1017/pasa.2026.10224 Published online by Cambridge University Press

Table A1. Continued.

TNS name					Original PATH		Marnoch23		Loudas25		Naive	
RA_{cand}	Dec_{cand}	θ	ϕ	mag	$P(U)$	$P(U\|\mathbf{x})$	$P(U)$	$P(U\|\mathbf{x})$	$P(U)$	$P(U\|\mathbf{x})$	$P(U)$	$P(U\|\mathbf{x})$
(deg)	(deg)	(")	(")		$P(O)$	$P(O\|\mathbf{x})$	$P(O)$	$P(O\|\mathbf{x})$	$P(O)$	$P(O\|\mathbf{x})$	$P(O)$	$P(O\|\mathbf{x})$
FRB20240201A					0.100	0.046	0.001	0.000	0.025	0.000	0.004	0.000
149.9062	14.0888	3.76	5.00	16.92	0.900	0.954	0.052	1.000	0.049	1.000	0.049	1.000
FRB20240210A					0.100	0.282	0.000	0.000	0.014	0.000	0.002	0.000
8.7770	−28.2721	9.42	6.42	15.13	0.758	0.718	0.037	1.000	0.033	1.000	0.034	1.000
FRB20240304A					0.100	0.008	0.034	0.003	0.055	0.003	0.032	0.002
136.3305	−16.1662	1.84	0.97	21.08	0.900	0.992	0.137	0.997	0.205	0.997	0.183	0.998
FRB20240310A					0.100	0.002	0.023	0.000	0.050	0.000	0.025	0.000
17.6219	−44.4393	0.39	1.06	20.16	0.687	0.997	0.109	0.999	0.201	0.999	0.137	0.999
17.6228	−44.4387	3.66	0.93	21.80	0.141	0.001	0.177	0.001	0.160	0.001	0.201	0.001

https://doi.org/10.1017/pasa.2026.10224 Published online by Cambridge University Press